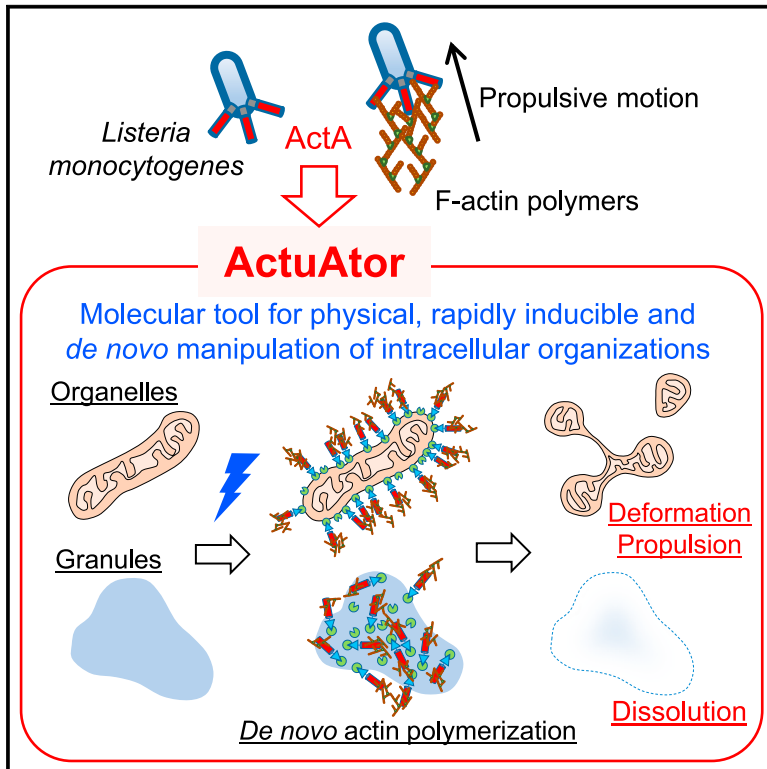


# ActuAator, a *Listeria*-inspired molecular tool for physical manipulation of intracellular organizations through *de novo* actin polymerization

## Graphical abstract



## Authors

Hideki Nakamura, Elmer Rho, Christopher T. Lee, ..., Padmini Rangamani, Shigeki Watanabe, Takanari Inoue

## Correspondence

nakamura@sbchem.kyoto-u.ac.jp (H.N.), jctinoue@jhmi.edu (T.I.)

## In brief

Inspired by bacterial tactics for survival, Nakamura et al. develop a molecular tool termed ActuAator that enables actin polymerization at intended locations in cells. The ActuAator targeted to organelles triggers their deformation, movement, and/or dissolution, offering one of the few ways to reveal the form-function interplay of subcellular organizations.

## Highlights

- Nakamura et al. develop a series of molecular tools termed ActuAator
- ActuAator can achieve *de novo* actin polymerization inside living cells
- ActuAator deforms membrane-bound organelles while dispersing molecular condensates
- ActuAator directly tests causal form-function relationships of organelles such as mitochondria



## Article

# ActuA<sub>tor</sub>, a *Listeria*-inspired molecular tool for physical manipulation of intracellular organizations through *de novo* actin polymerization

Hideki Nakamura,<sup>1,2,3,\*</sup> Elmer Rho,<sup>1</sup> Christopher T. Lee,<sup>4</sup> Kie Itoh,<sup>1</sup> Daqi Deng,<sup>1</sup> Satoshi Watanabe,<sup>1</sup> Shiva Razavi,<sup>5</sup> Hideaki T. Matsubayashi,<sup>1</sup> Cuncheng Zhu,<sup>4</sup> Eleanor Jung,<sup>4</sup> Padmini Rangamani,<sup>4</sup> Shigeki Watanabe,<sup>1</sup> and Takanari Inoue<sup>1,5,6,\*</sup>

<sup>1</sup>Department of Cell Biology and Center for Cell Dynamics, Johns Hopkins University School of Medicine, Baltimore, MD 21205, USA

<sup>2</sup>Kyoto University Hakubi Center for Advanced Research, Yoshida-honmachi, Sakyo-ku, Kyoto 606-8501, Japan

<sup>3</sup>Kyoto University Graduate School of Engineering, Department of Synthetic Chemistry and Biological Chemistry, Katsura Int'tech Center, Graduate School of Engineering, Kyoto University, Nishikyo-ku, Kyoto 615-8530, Japan

<sup>4</sup>Department of Mechanical and Aerospace Engineering, University of California San Diego, La Jolla, CA 92093, USA

<sup>5</sup>Department of Biomedical Engineering, Johns Hopkins University School of Medicine, Baltimore, MD 21205, USA

<sup>6</sup>Lead contact

\*Correspondence: [nakamura@sbchem.kyoto-u.ac.jp](mailto:nakamura@sbchem.kyoto-u.ac.jp) (H.N.), [jctinoue@jhmi.edu](mailto:jctinoue@jhmi.edu) (T.I.)

<https://doi.org/10.1016/j.celrep.2023.113089>

## SUMMARY

Form and function are often interdependent throughout biology. Inside cells, mitochondria have particularly attracted attention since both their morphology and functionality are altered under pathophysiological conditions. However, directly assessing their causal relationship has been beyond reach due to the limitations of manipulating mitochondrial morphology in a physiologically relevant manner. By engineering a bacterial actin regulator, ActA, we developed tools termed “ActuA<sub>tor</sub>” that inducibly trigger actin polymerization at arbitrary subcellular locations. The ActuA<sub>tor</sub>-mediated actin polymerization drives striking deformation and/or movement of target organelles, including mitochondria, Golgi apparatus, and nucleus. Notably, ActuA<sub>tor</sub> operation also disperses non-membrane-bound entities such as stress granules. We then implemented ActuA<sub>tor</sub> in functional assays, uncovering the physically fragmented mitochondria being slightly more susceptible to degradation, while none of the organelle functions tested are morphology dependent. The modular and genetically encoded features of ActuA<sub>tor</sub> should enable its application in studies of the form-function interplay in various intracellular contexts.

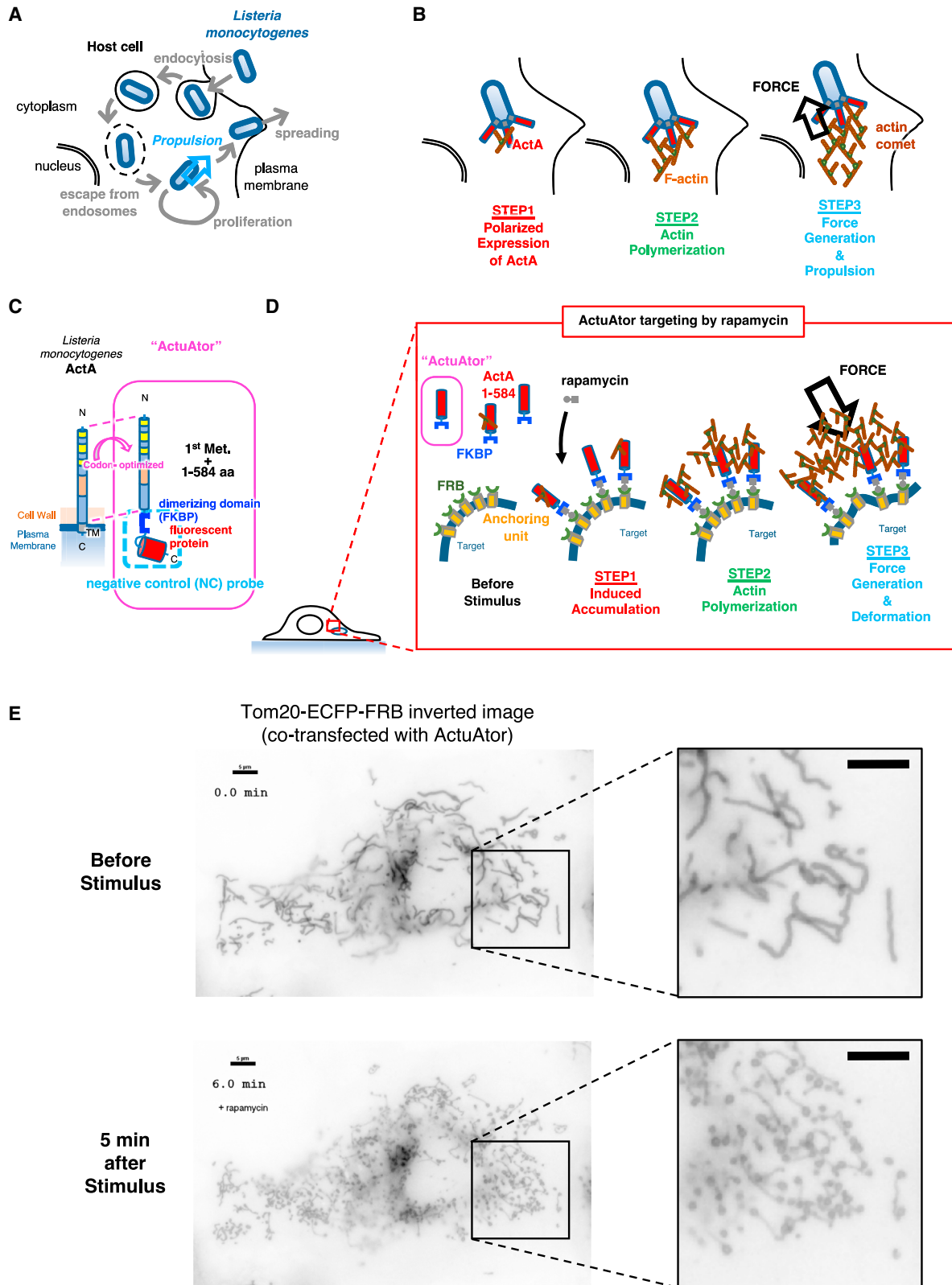
## INTRODUCTION

Every phenomenon in nature is ruled by the mechanical laws of physics. Living organisms are no exception. Mechanical force regulates diverse physiological processes including development,<sup>1</sup> gene expression,<sup>2</sup> differentiation,<sup>3</sup> and organelle morphology,<sup>4,5</sup> as well as pathophysiological processes such as cancer.<sup>6,7</sup> While cellular mechanoresponses have been studied mostly at the cell surface, there is accumulating evidence of mechanoresponses at play inside cells.<sup>5,8</sup> As such, there have been efforts to establish physical techniques for force manipulation at the cellular and subcellular levels.<sup>9–12</sup> However, most previous techniques have difficulty in directing physical probes against intracellular structures deep inside cells, limiting their intracellular applications to a few examples.<sup>13,14</sup> Moreover, their throughput is low, typically limited to a single location of force exertion at a time. Some studies adopt biologic probes such as living bacteria<sup>5</sup> or engineered proteins<sup>15–17</sup> to circumvent the challenge. Living bacteria deformed mitochondria by directly pushing the organelle, while feasible spatiotemporal control is

lacking. Protein-based probes, especially engineered motor proteins,<sup>15,16</sup> enabled controlled movement of intracellular organelles to inducibly manipulate their distributions, but drastic deformation of intracellular structures has been out of reach. Generalizable techniques to target specific arbitrary intracellular structures to move and deform them are thus still anticipated to elucidate the form-function relationship of intracellular structures, which may play essential roles in intracellular mechanobiological processes.

In microbiology, pathogenic microorganisms such as *Listeria* and *Shigella* are known to exercise unique strategies to facilitate their infection efficiency<sup>18</sup>; they hijack the host's actin machinery to move around and deform membrane structures in host cells. For example, *Listeria* utilizes a protein ActA on its surface,<sup>19,20</sup> which “impersonates” host actin nucleation-promoting factors.<sup>21–23</sup> The resulting actin polymerization generates force, enabling bacteria to propel through the host cytosol and eventually penetrate the plasma membranes for further infections. The model of the underlying force for the ActA-driven motility has been demonstrated theoretically<sup>24</sup> as well as experimentally,





(legend on next page)

ranging from studies *in situ*<sup>25</sup> to *in vitro* reconstitution with purified proteins.<sup>26,27</sup> We envisioned the potential of this bacterial strategy of hijacking actin polymerization machinery in developing a molecular tool for the study of the form-function relationship of intracellular structures.

## RESULTS

### A novel bacteria-inspired tool deformed and moved mitochondria in an inducible manner

In developing a molecular tool that can generate *de novo* force inside living cells in a well-controlled manner, we begin by describing how an infectious bacterium, *Listeria monocytogenes*, moves around inside host cells for its efficient proliferation (Figure 1A). Here, a single transmembrane protein, ActA, plays a critical role in generating bacterial motility<sup>19,20</sup> (Figure 1B). As a mimic of actin nucleation-promoting factors such as N-WASP and WAVE, ActA utilizes the host cell Arp2/3, as well as the ensuing Arp2/3 dependent actin polymerization<sup>23</sup> (Figure 1B). Confined expression of ActA to the posterior half of bacteria leads to polarized actin polymerization, which in turn generates directional force onto the bacteria, resulting in directed, thus efficient, propulsion.<sup>22,24,26,28</sup>

Inspired by the bacterial hijacking strategy, we speculated that ActA could be rationally engineered to enable *de novo* force generation in mammalian cells through induction of ectopic actin polymerization. More specifically, we aimed to rapidly and inducibly concentrate ActA-derived peptide at an intended intracellular target by employing chemically inducible dimerization (CID) where chemical administration triggers protein-protein interaction.<sup>29</sup> We fused a soluble and minimally functional fragment of ActA to one of the dimerizing proteins (FKBP), while linking the other half of the dimerizing pair (FRB) to a target sequence to confine its expression to a specific subcellular location. We thereby intended to stimulate interaction between the two dimerizing proteins upon addition of a chemical dimerizer (rapamycin), which should result in the accumulation of the engineered ActA.

Toward this end, we first codon optimized the extracellular domain of original ActA (1–584 amino acids [aa]) to improve the poor expression of bacterial sequence in mammalian cells,

and fused the codon-optimized peptide with FKBP and a fluorescent protein, mCherry (Figure 1C). We confirmed efficient induction of actin polymerization by the peptide by *in vitro* pyrene assay (Figure S1A). Accordingly, mere overexpression of the modified ActA peptide increased the amount of polymerized actin, while the effect was rather modest (Figure S1B). We further investigated the functionality of this modified ActA in cells by inducibly accumulating the peptide at the plasma membrane using the CID scheme. As a result, we observed an increase in actin-rich microspikes at the cell periphery (Figure S1C), consistent with constitutive expression of plasma membrane-targeted ActA.<sup>30</sup> We also evaluated the effect of ActA expression on cellular viability using a fluorometer-based assay, and we observed a negligible amount of cell death, which is comparable to other negative controls (NCs) (Figure S1D), suggesting little to no cytotoxicity. We hereafter refer to the recruitable ActA-based molecular probe as ActuAtoR (Figure 1D).

As an initial evaluation of the tool, we targeted mitochondria with ActuAtoR by co-expressing ActuAtoR and FRB fused to a mitochondria-targeting peptide derived from Tom20. Upon ActuAtoR accumulation in response to rapamycin addition, mitochondria morphology changed from tubular to an apparently punctate, vesicular shape within 5 min (Figure 1E; Video S1). This rapid and drastic change in morphology was accompanied by the movement of vesicular-shaped mitochondria, which further suggested successful force generation by ActuAtoR.

### ActuAtoR deformed mitochondria through actin polymerization

We characterized the mechanism of the mitochondria deformation by simultaneously monitoring actin polymerization using F-actin marker, Lifeact, co-expressed in the same cell (Figure 2A, left panels; Video S2). To quantify the observed morphological changes, we measured both area and perimeter length of mitochondria based on the Tom20-ECFP-FRB fluorescence signals at each time point. A morphometric parameter was then calculated by dividing the perimeter length by the area. By plotting the morphometric parameters, along with fluorescence intensity of Lifeact and ActuAtoR, as a function of time, we could visualize sequential development of each event one after another, specifically in the order of ActuAtoR accumulation, actin

#### Figure 1. A novel tool, ActuAtoR, was developed based on a bacterial protein ActA

(A) Life cycle of *Listeria monocytogenes* in host cells. *Listeria* invades into the cytosol by endocytic entry into host cells followed by escape from endosomes. They proliferate in the cytosol and move around by hijacking actin polymerization of the host cell. The propulsion process is essential for the bacteria to escape from the host cell to spread across other cells in the tissue.

(B) Mechanism of *Listeria* propulsion in the host cell cytosol. A bacterial membrane protein, ActA, is essential for the process. In the host cell cytosol, *Listeria* expresses ActA in a polarized manner (left panel). Extracellular domain of ActA then induces polymerization of host cell actin by functionally mimicking actin nucleation promoting factors of the host cell (middle panel). The polymerized actin polarization generates directional force exerted onto the bacteria, propelling them in the cytosol to realize bacterial motion (right panel).

(C) Schematic drawing of the engineered peptide, termed ActuAtoR, derived from ActA. Extracellular domain of original ActA was codon-optimized for mammalian expression and was fused to a dimerizing domain (blue) and a fluorescent protein (red). An NC peptide that lacks the ActA-derived domain (NC probe, highlighted by cyan broken line) was used in the following experiments. Basic characterization of ActA-derived domain, including actin polymerization-inducing ability, was performed *in vitro* and *in cellulo* (Figure S1).

(D) Design of a novel force-generating tool, ActuAtoR. An engineered peptide depicted in (C) was accumulated onto the target, leading to actin polymerization that generates force.

(E) Morphology of mitochondria in a COS-7 cell before (upper panels) and after rapamycin addition (lower panels) are shown as inverted fluorescence intensity images of a mitochondria marker, Tom20-ECFP-FRB. ActuAtoR targeted to mitochondria drastically deformed the organelle within 5 min. Zoomed images are shown in right panels. Scale bars, 5  $\mu$ m. Full version of the same data is provided as Video S1.

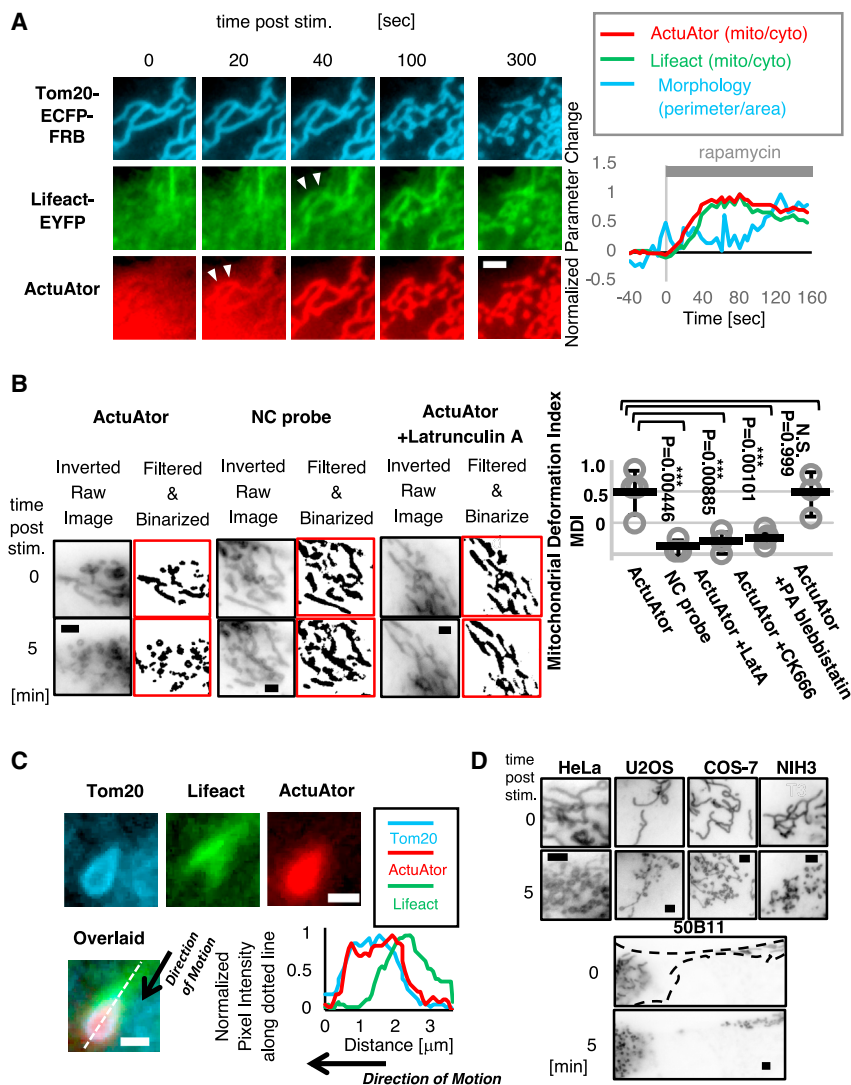


**Figure 2. Actuator inducibly generates force inside living cells to deform mitochondria**

(A) Left: mitochondria deformation in a U2OS cell shown as sequential images of Tom20-ECFP-FRB (mitochondria marker, cyan), Lifeact-EYFP (F-actin marker, green), and Actuator (red images). Scale bar, 2  $\mu$ m. Right: normalized ratio between Actuator signal intensity at mitochondria and in the cytosol (red), same ratio of Lifeact signal (green), and normalized ratio between number of pixels at the perimeter and number contained in the entire area of binarized mitochondria image (cyan) are plotted. Full version of the same data is provided as [Video S2](#).

(B) Left: mitochondria morphology in HeLa cells before (upper panels, 0 min) and 5 min after (lower panels, 5 min) rapamycin addition shown as inverted images (Inverted Raw Image) and as images binarized following top-hat morphology filtering (filtered and binarized). Scale bars, 2  $\mu$ m. Right: mitochondrial deformation index (MDI) is defined as [Equation 1](#) in the main text. MDI values 5 min after stimuli were plotted (N = 3, 4, 3, 4, 3, from left to right, respectively). Single data samples are plotted as gray circles and mean  $\pm$  standard deviation values as black markers. Statistical analysis was by Tukey honestly significant difference (HSD) test. \*\*\*p < 0.01; N.S., not significant. Images of CK-666- and PA-blebbistatin-treated cells are shown in [Figures S2A](#) and [S2B](#), respectively. Accumulation of Arp2/3 at the polymerization site is shown in [Figure S2C](#). Mitochondrial deformation efficiency of Actuator is compared with other actin nucleators in [Figure S2D](#).

(C) Deformed vesicular-shaped mitochondria move with trailing polymerized actin comet. Fluorescence images of a single moving vesicle are shown separately in the left panels. Overlaid image and line-scan plot along the white broken arrow in the right panels indicate polymerized actin tail seen in green Lifeact channel is behind the vesicle. Scale bar, 1  $\mu$ m.

(D) Actuator-induced mitochondrial deformation was evaluated in five distinct cell lines, HeLa (cervix derived, epithelial-like), U2OS (bone derived, epithelial-like), COS-7 (kidney derived, fibroblast- or

endothelial-like), NIH-3T3 (fibroblast derived, fibroblast-like), and 50B11 (dorsal root ganglion neuron derived, neuron-like) cells. Inverted fluorescence images of Tom20-ECFP-FRB right before (0 min) and 5 min after stimulus (5 min) are shown for each cell line. Scale bars, 2  $\mu$ m. Further characterization is shown in [Figure S3](#).

polymerization, and then the organelle deformation ([Figure 2A](#), right panel). This order is consistent with the sequence of steps ActA takes to drive bacterial propulsion ([Figure 1B](#)) and what we designed for Actuator operation ([Figure 1D](#)). The deformation was not observed when FKBP without the ActA module (termed NC probe, [Figure 1C](#)) was used instead. To quantify this observation, we introduced another parameter for mitochondrial deformation (MDI) as defined by the following equation:

$$MDI = \frac{\text{mitochondria length before stimulus}}{\text{mitochondria length after stimulus}} \quad (\text{Equation 1})$$

With MDI calculations under different conditions, we confirmed the significant difference between Actuator and the NC probe ([Figure 2B](#)). Subsequent experiments using pharmacological inhibitors revealed that the Actuator-mediated deformation requires Arp2/3-dependent actin polymerization, but not myosin motors

([Figures 2B](#) and [S2A–S2C](#)). Using the mitochondria deformation as a model, we then compared Actuator with other actin nucleation-promoting factors and its regulators such as N-WASP, EspFu, and Nck ([Figures S2D](#) and [S2E](#)). As a result, Actuator outperformed the others. As mentioned earlier, deformed mitochondria with vesicular morphology often exhibited transient motion, featuring a polymerized actin comet tail similar to that observed with *Listeria* and in *in vitro* reconstitution studies<sup>31,32</sup> ([Figure 2C](#)). We also tested if Actuator can be widely used across different cell types and observed robust deformation of mitochondria in all five cell types tested ([Figure 2D](#)).

Actin polymerization has been implicated as a part of the physiological mitochondrial fission process through Drp1, a GTPase that executes mitochondria fission.<sup>33</sup> We therefore investigated the requirement of endogenous Drp1 for Actuator-induced deformation of mitochondria. We found that Actuator still



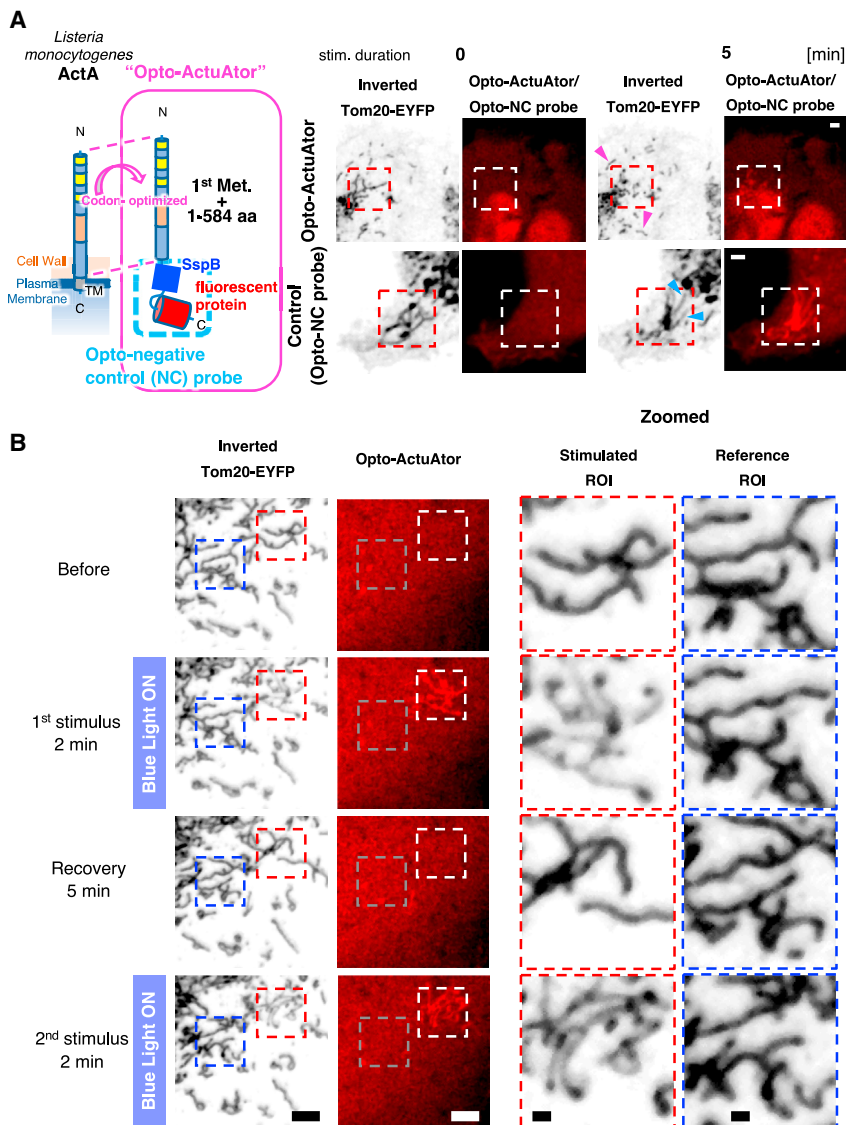


**Figure 3. Opto-ActuAtor improved spatiotemporal control of mitochondria deformation**

(A) Light-inducible Actuator enabled local deformation of mitochondria. Design of the tool is shown in the left panel. Actuator peptide was inducibly accumulated at mitochondrial surface by blue-light-dependent dimerization between SspB and iLID in a U2OS cell. The light was irradiated in the square region shown by broken lines. Light was irradiated immediately before each acquisition during the stimulus. Scale bars, 2  $\mu$ m.

(B) Repetitive and local deformation of mitochondria in U2OS cells by light. The same region of interest (ROI) (red broken-line square) was repeatedly stimulated. Mitochondria in stimulated ROI was deformed repetitively (stimulated ROI in zoomed panels, second and fourth panels from top) while no significant morphology change was observed in reference ROI (blue broken-line square, reference ROI in zoomed panels). Timing of the first and second stimulus is shown by blue bars on the left. Scale bars, 2  $\mu$ m in left panels, 1  $\mu$ m in zoomed panels.

The EM images indicated that the mitochondria maintained their membrane integrity despite the overall morphological changes (Figure S3D).

While CID allows for multicolor fluorescence imaging with ease, most CID tools are practically irreversible.<sup>36</sup> Also, chemical administration often lacks fine spatial control. To improve the spatiotemporal precision of the Actuator operation, we adapted light-inducible dimerization (LID)<sup>37</sup> to develop optogenetic Actuator probes (opto-Actuator). We employed a light-sensitive peptide, iLID, and its binding partner, SspB,<sup>38</sup> which we fused to a mitochondria-targeting sequence and the engineered ActA peptide, respectively. Upon blue light illumination in a sub-region of a target cell,

deforms mitochondria even in the absence of Drp1 (Figure S3A), implying that the mechanism is independent of endogenous mitochondria fission machinery.

We next assessed possible off-target effects of the tool by performing simultaneous imaging of other subcellular organizations during the Actuator operation at mitochondria. When we visualized stress fibers (Figure S3B) or endoplasmic reticulum (ER) (Figure S3C), little to no detectable change was observed within 5 min of rapamycin addition. This result suggested minimal side effects of the Actuator operation on actin-related structures, despite the utilization of actin machinery, and on non-targeted organelles despite the close proximity.<sup>34,35</sup>

To assess membrane integrity of the Actuator-deformed organelles, we performed correlative light and electron microscopy (CLEM) where we aimed to obtain an electron microscopy (EM) image of the exact cells that we observed to have undergone morphological changes under a fluorescence microscope.

opto-Actuator probes induced mitochondria deformation locally (Figure 3A) as well as reversibly and repetitively (Figure 3B).

### Actuator deformed versatile organelles

The modular molecular design of Actuator should enable its application to other organelles. We therefore directed the tool to Golgi apparatus using CID and a Golgi-targeting sequence derived from Giantin. Rapamycin triggered accumulation of Actuator at Golgi and subsequent morphological changes (Figure 4A; Video S3), which were not observed with an NC peptide probe (Figure 4B). Tracking Golgi morphology over time indicated a loss of dense spots within the Golgi cluster and its concomitant dispersion (Figure 4C). A top-hat morphology filter revealed small particles emanating from the Golgi cluster (Figure S4A). We also captured actin comet-like structures associated with these particles that were moving across the cytosol (Figure S4B).

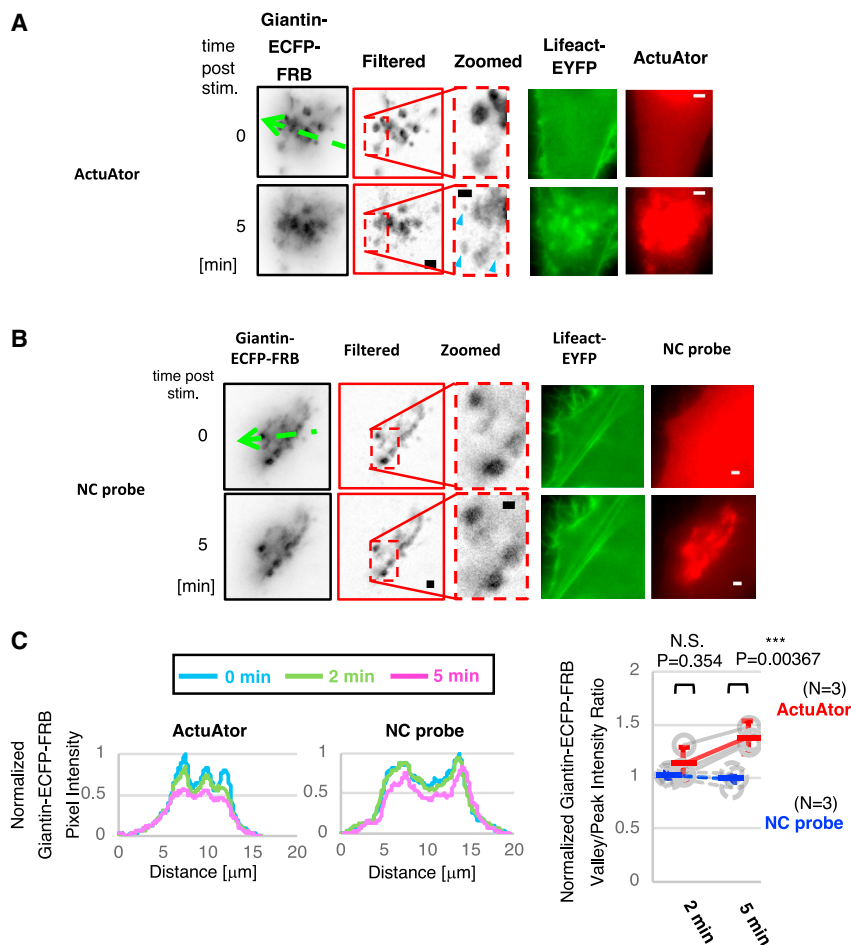


**Figure 4. ActuA deforms Golgi apparatus**

(A) Golgi marker (giantin-ECFP-FRB, inverted images), Lifeact (Lifeact-YFP, green), and ActuA (ActuA-FKBP-mCherry, red) images are shown before (0 min) and 5 min after stimulus (5 min). Golgi morphology was extracted by filtering the giantin-ECFP-FRB images by top-hat morphology filter (filtered, zoomed).

(B) Golgi apparatus morphology upon recruitment of the NC peptide without ActA-derived domains (NC probe) is shown in similar fashion as (A). Green arrows in broken lines indicate the positions of line-scan profiles shown in (C). Scale bars, 1  $\mu\text{m}$  in zoomed images, 2  $\mu\text{m}$  in other images.

(C) Left panels: normalized fluorescence intensity profiles along the green arrows (A) and Figure S9A are plotted. Right panel: ratio between the intensity values at the peak and those at the valley in the line-scan profiles are plotted. Results for each cell are plotted as gray circles with solid or broken lines, respectively. Red and blue markers are for cells with or without ActA-derived sequence, respectively. Statistical analysis was carried out with two-tailed Welch's t test. \*\*\* $p < 0.01$ ; N.S., not significant. Zoomed images of deformed Golgi apparatus are also shown in Figures S4A and S4B. Scale bars, 1  $\mu\text{m}$  in zoomed images, 2  $\mu\text{m}$  in other images.

Next, we applied ActuA to ER and outer nuclear envelope (ONE), using FRB fused to a targeting peptide, Sec61B. Upon chemical dimerization and recruitment of ActuA to these sites, the majority of cells exhibited one of three classes of actin-rich membrane deformation at ONE: ring-like patches (Figure 5A; Video S4), needle-like spikes (Figure 5B; Video S5), and finger-like protrusions (Figure 5C; Video S6). None of these phenotypes were observed when FKBP alone was used (NC probe; Figures 5D and 5E). Needle-like spikes have previously been observed in a cell-free system where actin was polymerized on the outer surface of a giant unilamellar vesicle.<sup>39</sup> While finger-like protrusions or ring-like patches have not been reported in cell-free systems, we speculated that all these three seemingly distinct morphologies may be the same object oriented at a different angle, or on a different confocal plane. This was confirmed to be the case based on the inspection of the entire nucleus reconstituted in three dimensions using confocal microscopy (Figure S4C).

To further estimate the force generated by ActuA, we developed a numerical approach that builds on recent work applying discrete differential geometry to membrane mechanics.<sup>40</sup> For this purpose, we extracted the morphology of the deformed nuclear envelope membrane with nanoscopic resolution using CLEM. Applying the Helfrich-Canham-Evans energy<sup>41,42</sup> and us-

ing strategies for automatic differentiation we estimate the forces generated by the membrane given its extracted shape. Assuming that the observed shape is at equilibrium, it must be balanced by an opposing force, which we assume to be produced by ActuA. We apply this

approach to the needle-like spike and estimated the maximal forces required to realize the degree of observed deformation to be 370  $\text{pN}/\mu\text{m}^2$  (Figure S4D, supplemental information). This value is compatible with the range of force required to move *Listeria in situ*<sup>43</sup> or the force generated by reconstituted F-actin networks *in vitro*.<sup>28,31,44</sup>

### Mitochondria form-function relationship

After demonstrating that ActuA can polymerize actin, generate force, and deform target structures, we aimed to implement the tool in assessing the form-function relationship of intracellular organelles. Mitochondria undergo cycles of fission and fusion, whose balance dictates overall morphology as an equilibrium state.<sup>45,46</sup> Interestingly, the shape of mitochondria appears to correlate with their function.<sup>47,48</sup> Long, filamentous mitochondria exhibit upregulation of oxidative phosphorylation, while fragmented mitochondria are associated with compromised functionality. Despite the significance, it has long been out of reach to test a causal relationship between mitochondrial morphology and functions, primarily because existing experimental approaches are limited in directly manipulating the morphology of this submicrometer length-scale entity inside cells. ActuA-mediated acute deformation of mitochondria presents one of the most straightforward approaches of

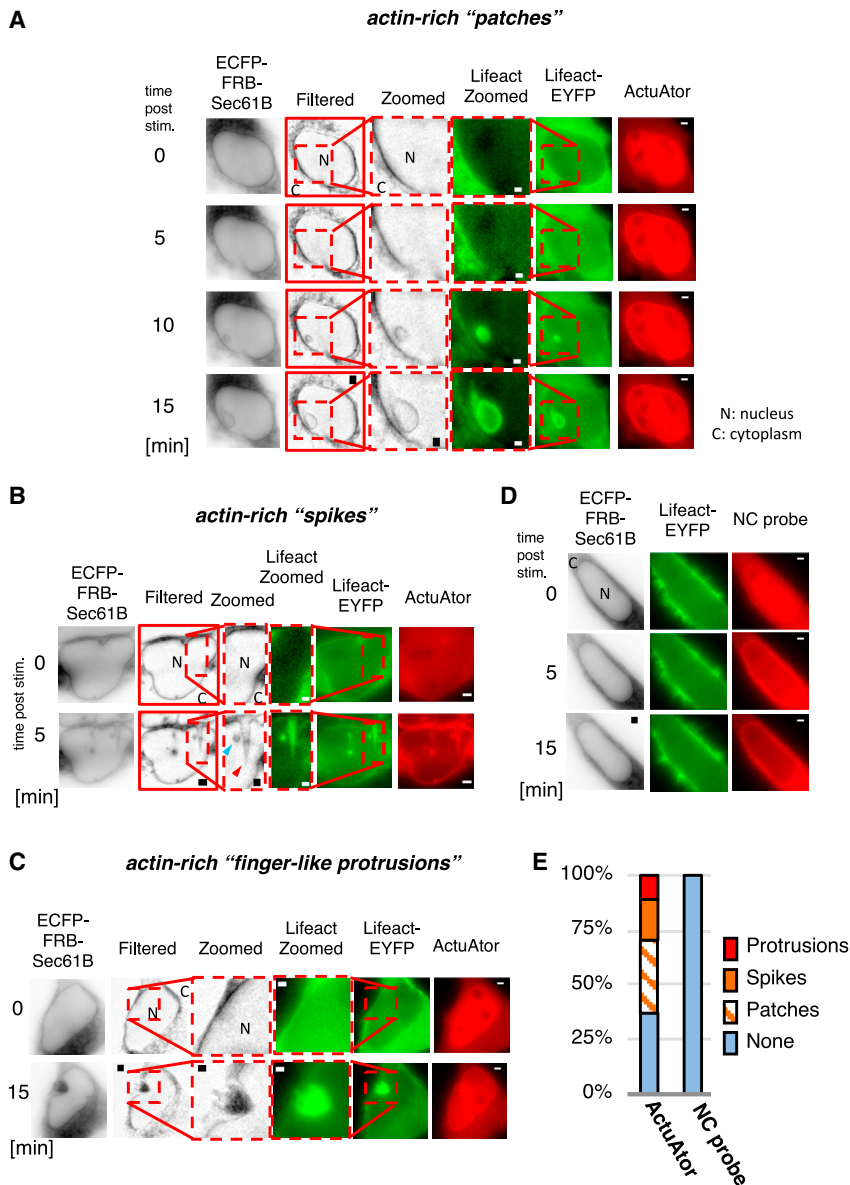


**Figure 5. ActuAtoR deforms outer nuclear envelope**

(A) A representative actin-rich patch found in deformed nucleus. Fluorescence images of ER and ONE marker (ECFP-FRB-Sec61B, shown as inverted images), Lifeact (Lifeact-EYFP, green), and ActuAtoR (ActuAtoR-FKBP-mCherry, red) are presented. ONE morphology extracted by top-hat morphology filter (filtered).

(B) Representative actin-rich spikes found in deformed nucleus.

(C) A representative actin-rich finger-like protrusion found in deformed nucleus.

(D) Accumulation of the NC peptide probe did not induce the morphological change in the nucleus.

(E) Fraction of the cells categorized in each phenotypic class (N = 27 and 22 for ActuAtoR and NC probe, respectively). It should be noted that each class most probably reflects a distinct region of the deformed nucleus. Three-dimensionally reconstituted high-resolution fluorescence image of a deformed nucleus is shown in Figure S4C. Correlative transmission electron microscopy (TEM) image as well as the result of force density distribution generated by ActuAtoR is shown in Figure S4D. Scale bars, 1  $\mu\text{m}$  in zoomed images, 2  $\mu\text{m}$  in other images.

perturbing "form" while allowing for assessment of its immediate effects on mitochondria functions. To begin examining the organelle form-function interplay, we first performed fluorescence recovery after photobleaching (FRAP) experiments to confirm the limited connectivity between two mitochondria that were fragmented via the ActuAtoR operation (Figure S5). The extent of connectivity was indistinguishable from that of mitochondria fragmented by treatment with cyanid *m*-chlorophenyl hydrazone (CCCP), a small-molecule protonophore that inhibits ATP synthesis in mitochondria.

We then measured representative mitochondria properties, synthesis of ATP, maintenance of membrane potential, and generation of reactive oxygen species (ROS) using fluorescent biosensors, mitochondria-targeted ATeam 1.03 (mitAT1.03),<sup>49</sup> tetramethylrhodamine ethyl ester (TMRE),<sup>50</sup> and mitochondria-

targeted HyperRed (HyperRed-mito),<sup>51</sup> respectively. Time-lapse fluorescence measurement was carried out for 15 min (5 min pre-stimulus and 10 min post stimulus) in two cell types, HeLa and Cos-7, which were cultured in either glucose- or galactose-containing medium. Replacement of glucose by galactose shifts the cellular energy source from cytosolic glycolysis to mitochondrial oxidative phosphorylation.<sup>52,53</sup>

As a result, mitochondrial ATP indicated a modest decrease shortly after mitochondria deformation under two out of four conditions (HeLa/gal, Cos-7/glu), while no detectable change was observed in the remaining two conditions (HeLa/glu, Cos-7/gal) (Figures 6A and S6A). In contrast, we did not observe a significant change in membrane potential (Figures 6B and S6B) or ROS (Figures 6C and S6C) except in one out of eight conditions (HeLa/glu, ROS). The extent of this change was modest (less than 10%), and the difference was not exaggerated by replacing glucose by galactose. From these short-term functional assays, a clear pattern in the relationship between mitochondrial morphology and functions did not emerge.

We next explored the long-term effect of mitochondria deformation on mitophagy, namely autophagy-dependent degradation of mitochondria.<sup>54</sup> In a previous study, hyperfused mitochondrial morphology due to Drp1 knockout was linked to reduced mitophagy, which was rescued by reversing



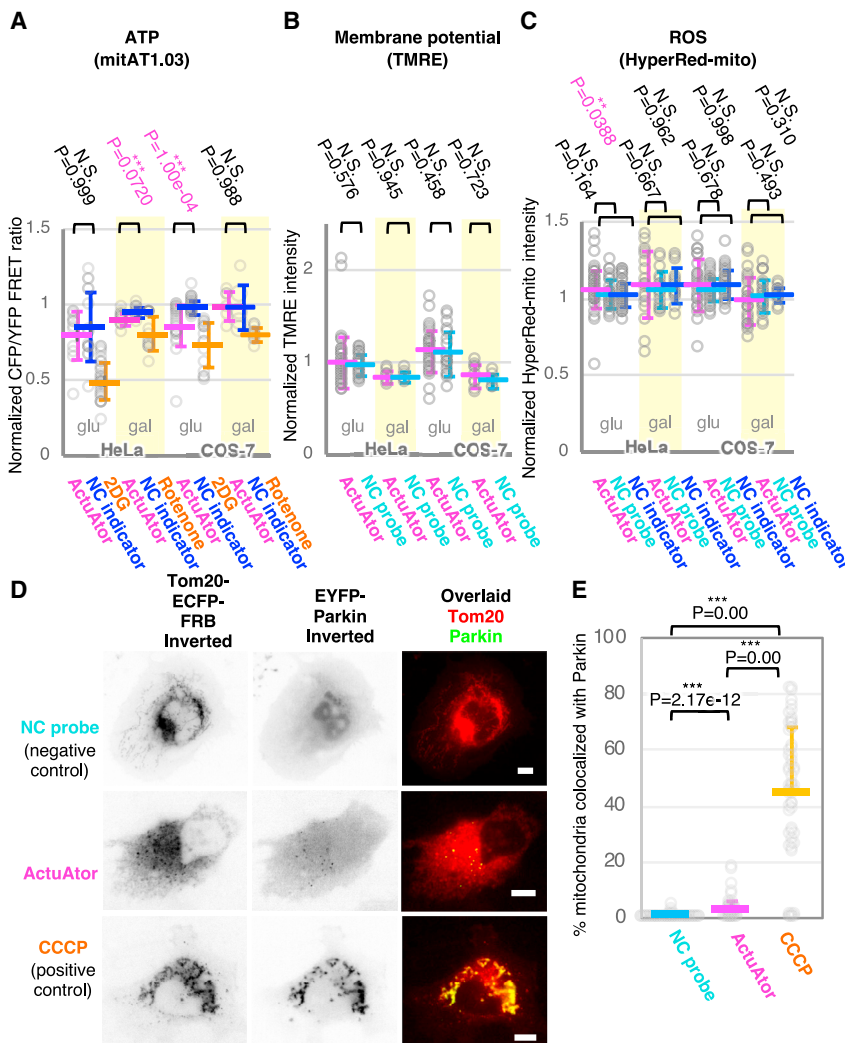


**Figure 6. Mitochondria deformation by ActuAator shows modest effects on mitochondrial functions**

(A–C) Effects of mitochondria deformation on mitochondria functions were evaluated by measuring three distinct parameters: ATP concentration at mitochondria, membrane potential across inner mitochondrial membrane, and reactive oxygen species (ROS) concentration at mitochondria. Statistical analyses on normalized signals 10 min after stimulus are shown as plots for mitochondrial ATP concentration (A), membrane potential (B), and mitochondrial ROS concentration (C). In all plots, magenta markers are the results with ActuAator. Results of cells cultured in galactose medium are highlighted by yellow backgrounds. Statistical analyses were done by Steel-Dwass test in (A) and (C) and by Mann-Whitney U test in (B). Connectivity between the deformed mitochondria was evaluated by fluorescence resonance energy transfer (FRET) measurement shown in Figure S5. Temporal evolution of the biosensor signals is shown in Figure S6. (D and E) Effects of mitochondria deformation on Parkin-dependent mitophagy. Colocalization of a mitochondria morphology marker (Tom20-ECFP-FRB) and EYFP-Parkin are shown as representative images (D) and quantified extent of colocalization in a plot (E). Scale bars, 5  $\mu$ m. Statistical analyses were done by Steel-Dwass test. In all plots, data points from individual cells are plotted as gray circles, while mean  $\pm$  standard deviation values are shown in markers. \*\*\* $p < 0.01$ .

the morphology via additional knockout of a fusion protein, Opa1.<sup>55</sup> To test how acute mitochondria deformation affects mitophagy, we performed an assay where the extent of colocalization between fluorescently labeled Parkin (EYFP-Parkin) and ActuAator-deformed mitochondria was measured as a readout of mitophagy. Twenty-four hours after the ActuAator operation, we observed a modest increase in colocalization (2.3%), while the NC with FKBP alone (NC probe) showed no increase, and the positive control of CCCP treatment induced 45% increase (Figures 6D and 6E). Although there may be an involvement of unexpected side effects of ActuAator operation such as actin polymerization, our results indicated that small, fragmented mitochondria became more susceptible to mitophagy.

### Synthetic dispersion of a physiological phase-separated condensate

To further explore the versatility of ActuAator, we aimed to deform other classes of intracellular organizations, namely non-membrane-bound biomolecular condensates.<sup>56,57</sup> These

structures are composed of multiple biomolecules, most typically proteins and RNAs, without any membranes defining their boundaries. While there are techniques available to induce assembly of biomolecules to form artificial condensates,<sup>58</sup> physiological roles of native condensates remain largely unknown due to the lack of techniques to manipulate them in their intact form.

As a benchmark, we chose stress granules, which are mRNA-containing condensates that are transiently formed in cells under various stresses<sup>59</sup> and are associated with neurodegenerative diseases such as amyotrophic lateral sclerosis.<sup>60</sup> We performed the ActuAator operation at stress granules that were induced to form in response to a chemical stress such as extracellular sodium arsenite. We first made an FRB fusion protein with a stress granule marker, TIA-1, which we co-expressed with the chemically inducible ActuAator. Upon addition of rapamycin, ActuAator was recruited to the stress granules, followed by actin polymerization throughout granules (Figure 7A; Video S7). Strikingly, stress granules were dispersed over time in the continuous presence of sodium arsenite. Unexpectedly, when an NC peptide FKBP alone with no ActA portion (NC probe) was accumulated at the stress granules, we also observed dispersion of the granules (Figure S7A), albeit to a moderate extent and frequency. This background effect could be due to molecular crowding at the granule weakening the molecular interactions within. We next replaced

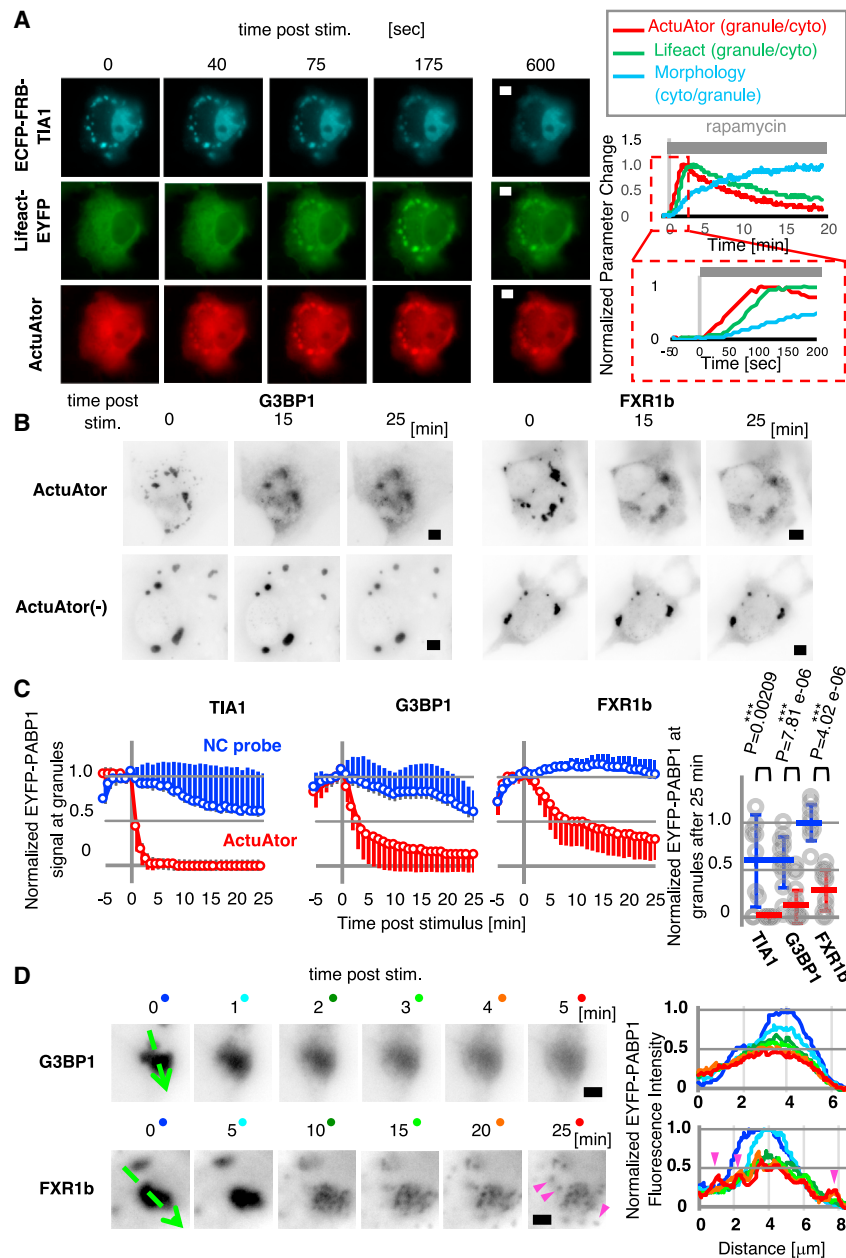


**Figure 7. ActuAator disperses a non-membrane-bound condensate, stress granules**

(A) Fluorescence images of stress granule morphology marker (ECFP-FRB-TIA1, cyan), Lifeact (Lifeact-EYFP, green), and ActuAator peptide (ActuAator-FKBP-mCherry) at distinct time points are shown in the left panel. Scale bars, 5  $\mu$ m. In the right panel, normalized ratio of fluorescence intensities of ActuAator (red), Lifeact (green), and ECFP-FRB-TIA1 (cyan) at the granules to those in the cytosol are plotted against time. Enlarged plot is shown below in red broken-line rectangle for earlier time points. Representative time-lapse images of stress granules monitored by an independent marker, PABP1, are shown in Figure S7A.

(B) Multiple stress granule markers can be used to recruit ActuAator for inducible dispersion of granules. Stress granule morphology as inverted fluorescence intensity images of an independent stress granule marker, EYFP-PABP1, is shown. Two stress granule markers, G3BP1 and FXR1b, were used to recruit ActuAator to the granules, as ECFP-FRB-G3BP1 and ECFP-FRB-FXR1b, respectively. Both markers recruited ActuAator successfully, resulting in significant stress granule dispersion (ActuAator) compared to NC probe. Scale bars, 5  $\mu$ m.

(C) Left panel: temporal evolution of integrated fluorescence signal of a marker, EYFP-PABP1, at the granules with (ActuAator, red) or without ActuAator recruitment (NC probe, blue). Normalized signals are plotted for three stress granule markers, TIA-1, G3BP1, and FXR1b, used to inducibly accumulate the peptides. N = 10 regions from five cells (NC probe, TIA1), 10 regions from five cells (ActuAator, TIA1), 15 regions from 12 cells (NC probe, G3BP1), 23 regions from 12 cells (ActuAator, G3BP1), nine regions from five cells (NC probe, FXR1b), and 13 regions from six cells (ActuAator, FXR1b). Right panel: normalized integrated signals 25 min after stimulus are plotted for distinct conditions. Results in individual cells are plotted as gray circles, while mean  $\pm$  standard deviation values are shown in red and blue markers for cells with or without ActuAator. Statistical analysis was done by Mann-Whitney U test. \*\*\*p < 0.01.

(D) Difference in stress granule morphology during the dispersion by ActuAator recruited by distinct marker proteins. Inverted EYFP-PABP1 fluorescence images in a representative region at distinct time points are shown for each condition, where ECFP-FRB-G3BP1 (G3BP1) or ECFP-FRB-FXR1b

(FXR1b) was used to recruit ActuAator. In the right panel, line-scan profiles of the fluorescence intensity along green broken-line arrows are presented in colors corresponding to those of dots shown besides images in the left panel. FXR1b-dependent recruitment resulted in more distinguishable fragments, highlighted by magenta arrowheads in both panels. Scale bars, 2  $\mu$ m. Schematic drawing of ActuAator-dependent dispersion of condensates including stress granules is shown in Figure S7B, in comparison with the deformation of membrane-bound organelles.

TIA-1 with two other stress granule markers, G3BP1 and FXR1b, and characterized their efficiency, expecting to observe a different degree of the background effect. When we co-expressed either FRB fusion protein, CFP-FRB-G3BP1 or CFP-FRB-FXR1b, with ActuAator, rapamycin addition led to accumulation of ActuAator at the stress granules, followed by dispersion (Figure 7B). To quantify the extent of the stress granule dispersion with the three different FRB-fused anchors, we introduced EYFP-PABP1 as a stress granule marker whose fluorescence intensity at each time point

was normalized by their intensity value at time 0 (red lines, Figure 7C). The dispersion kinetic plot indicated that TIA-1 is most efficient, followed by G3BP1 and then by FXR1b. We also analyzed dispersion using an NC probe, FKBP alone (NC probe), which also indicated variations (blue lines, Figure 7C). Compared to TIA-1, G3BP1 induced slower dispersion, while FXR1b triggered almost no dispersion in NC experiments. Further characterization by monitoring the morphology of stress granules revealed a qualitative difference between marker proteins adopted: while

G3BP1 uniformly dispersed across a stress granule with an increasingly smooth edge, FXR1b broke it into smaller fragments that were clearly visible under the microscope (Figure 7D). The different characteristics of the stress granule dispersion could be attributed to the differential distribution of these anchor proteins within granules and/or to the distinct effects on biophysical properties of stress granules due to protein overexpression. The precise mechanism of the stress granule dispersion remains to be understood (Figure S7B). Although stress granules are one of the best-studied examples of non-membrane-bound organelles, their physiological functions are still under active debate. By uniquely perturbing structural organization of stress granules in an acute manner, Actuator may become helpful in uncovering the relationship among biomolecular assembly state, biochemical and biophysical properties, and biological functions.

## DISCUSSION

To our knowledge, Actuator is one of the few molecular tools that generate driving force to induce deformation of intracellular structures in a spatio-temporally controlled, target-specific, and rapidly inducible manner with measurable throughput. Other techniques, including optical and magnetic tweezers, are powerful as they exert physical forces of a predetermined strength, albeit at the expense of a low throughput and difficulty of directing the force to specific organelles.

The mechanism underlying the actin polymerization-dependent force generation by Actuator has been studied *in situ*, *in vitro*, and in theoretical considerations, using *Listeria*-derived protein ActA, on which the design of Actuator is based. Nevertheless, a sound understanding of the process should be advantageous, enabling rational improvement and application of the tool. Furthermore, the modular molecular design allows for further expansion of the list of target objects to be deformed in cells. Its genetically encoded nature also enables *in vivo* applications in the future. The concentration of Actuator probes and actin polymers may be titrated in cell-free membrane systems such as lipid vesicles in relation to the degree of deformation to infer the force amount, taking advantage of rich insights through previous studies. It would be interesting to change experimental parameters (rapamycin concentration, intensity and/or spatial patterns of light irradiation, expression level and ratio of FKBP/FRB or SspB/iLID constructs, etc.) to vary force amount and see if and how this correlates with the type of organelle deformation.

One area of major interest is to further explore the form-function correlation of organelles using Actuator. Mitochondria are particularly attractive, as their altered morphology is often observed under pathophysiological conditions such as heart failure, Alzheimer's disease, and Charcot-Marie-Tooth disease. Whether the deformed mitochondria are a cause or consequence of the pathological toxicity, and whether correction of morphology ameliorates symptoms, may be addressed by Actuator in the future. In all, Actuator will begin enabling fine examination of intracellular mechanobiology events.

## Limitations of the study

The observed deformation and movement of organelles induced by Actuator strongly imply generation of constrictive force as a

cause of the ensuing alterations. While this is partly supported by our biophysical modeling, direct measurement of mechanical force has to precede a definite conclusion. Likewise, it is unclear exactly what physical/biochemical principles are at play for the stress granule dispersion. Those outstanding points will be addressed in the near future using physical techniques applicable to the intracellular milieu, or perhaps with *in vitro* reconstituted systems where more broad physical methods could be readily applied.

## STAR★METHODS

Detailed methods are provided in the online version of this paper and include the following:

- **KEY RESOURCES TABLE**
- **RESOURCE AVAILABILITY**
  - Lead contact
  - Materials availability
  - Data and code availability
- **EXPERIMENTAL MODEL AND STUDY PARTICIPANT DETAILS**
  - Cell lines used in the study
- **METHOD DETAILS**
  - DNA plasmids
  - 6xHis-ActA (1–584)-FRB-CFP purification
  - *In vitro* pyrene assay of actin nucleation efficiency
  - Cell viability assay using FACS and cell viability dye
  - Transfection and live-cell imaging
  - Quantification of mitochondria deformation
  - Confocal imaging and optogenetic stimulation
  - Three-dimensional confocal imaging
  - Correlative electron microscopy
  - Estimation of force generated by Actuator
  - FRAP measurement and analysis
  - Fluorescence imaging of mitochondria functions
  - Stress granule dispersion
  - Quantification and statistical analysis

## SUPPLEMENTAL INFORMATION

Supplemental information can be found online at <https://doi.org/10.1016/j.celrep.2023.113089>.

## ACKNOWLEDGMENTS

The authors thank the following researchers for sharing research reagents: Hiroomi Imamura for Ateam1.03 constructs, Vsevolod Belousov for HyperRed constructs, Nancy Kedersha for stress granule-related constructs, Charlotte Sumner for 50B11 cells, and Hiromi Sasaki for Drp1 knockout cells and Parkin construct. Our appreciation is extended to Jodi Nunnari and Nancy Kedersha for experimental assistance and insightful discussions, Erin Goley for providing *in vitro* experimental environments as well as fruitful discussion, Brett Andrew McCray for technical advices on experiments, Aravind Chandrasekaran for insights on actin biophysics, Itaru Hamachi and Hiroshi Nonaka for providing experimental environments for advanced imaging and analysis, and to our lab members, including Brian Huang and Robert DeRose, for experimental assistance and fruitful discussions. We acknowledge support from JST PRESTO (JP21460382 to H.N.), JSPS KAKENHI (JP21H00397, JP22H05087, and JP22H05091 to H.N.), The Mochida Memorial Foundation for Medical and Pharmaceutical Research to H.N., the National Institutes of Health

(R01GM123130, R01GM136858, and R35 GM149329 to T.I.), HFSP research grant (RGP0026/2020 to T.I.), and the DoD DARPA (HR0011-16-C-0139 to T.I.). Shigeki Watanabe and K.I. are supported by the National Institutes of Health (1DP2 NS111133-01 and 1R01 NS105810-01A1). Shigeki Watanabe is a foundation scholar of Alfred P. Sloan, McKnight, Klingenstein and Simons, and Vallee. C.T.L. is supported by a Kavli Institute for Brain and Mind Postdoctoral Award. C.T.L., C.Z., E.J., and P.R. are supported by AFOSR MURI FA9550-18-1-0051 to P.R.

#### AUTHOR CONTRIBUTIONS

H.N. conceived the original design of Actuator. H.N. and T.I. designed experiments and wrote the manuscript. H.N. performed the majority of experiments and data analysis thereof, with the help of H.T.M. and Satoshi Watanabe. E.R. performed some of the mitochondria experiments and D.D. performed some of the stress granule experiments, both under the supervision of H.N. and T.I. H.T.M. performed and analyzed *in vitro* experiments using proteins purified by S.R. Shigeki Watanabe and K.I. prepared the cell culture samples and performed EM and CLEM analysis on fragmented mitochondria as well as deformed nuclei. C.T.L. estimated the forces by developing a biophysical model with help from C.Z. and E.J., which was conducted under the supervision of P.R. T.I. oversaw the project.

#### DECLARATION OF INTERESTS

The authors declare no competing interests.

#### INCLUSION AND DIVERSITY

We support inclusive, diverse, and equitable conduct of research.

Received: June 21, 2023

Revised: August 8, 2023

Accepted: August 21, 2023

Published: September 20, 2023

#### REFERENCES

- Mammoto, T., Mammoto, A., and Ingber, D.E. (2013). Mechanobiology and developmental control. *Annu. Rev. Cell Dev. Biol.* *29*, 27–61. <https://doi.org/10.1146/annurev-cellbio-101512-122340>.
- Shivashankar, G.V. (2019). Mechanical regulation of genome architecture and cell-fate decisions. *Curr. Opin. Cell Biol.* *56*, 115–121. <https://doi.org/10.1016/j.cob.2018.12.001>.
- Vining, K.H., and Mooney, D.J. (2017). Mechanical forces direct stem cell behaviour in development and regeneration. *Nat. Rev. Mol. Cell Biol.* *18*, 728–742. <https://doi.org/10.1038/nrm.2017.108>.
- Isermann, P., and Lammerding, J. (2013). Nuclear mechanics and mechanotransduction in health and disease. *Curr. Biol.* *23*, R1113–R1121. <https://doi.org/10.1016/j.cub.2013.11.009>.
- Helle, S.C.J., Feng, Q., Aebersold, M.J., Hirt, L., Grüter, R.R., Vahid, A., Sirianni, A., Mostowy, S., Snedeker, J.G., Šarić, A., et al. (2017). Mechanical force induces mitochondrial fission. *Elife* *6*, e30292. <https://doi.org/10.7554/eLife.30292>.
- Ingber, D.E. (2003). Mechanobiology and diseases of mechanotransduction. *Ann. Med.* *35*, 564–577.
- Suresh, S. (2007). Biomechanics and biophysics of cancer cells. *Acta Biomater.* *3*, 413–438. <https://doi.org/10.1016/j.actbio.2007.04.002>.
- Elosegui-Artola, A., Andreu, I., Beedle, A.E.M., Lezamiz, A., Uroz, M., Kosmalska, A.J., Oria, R., Kechagia, J.Z., Rico-Lastres, P., Le Roux, A.-L., et al. (2017). Force Triggers YAP Nuclear Entry by Regulating Transport across Nuclear Pores. *Cell* *171*, 1397–1410.e14. <https://doi.org/10.1016/j.cell.2017.10.008>.
- Iskratsch, T., Wolfenson, H., and Sheetz, M.P. (2014). Appreciating force and shape—the rise of mechanotransduction in cell biology. *Nat. Rev. Mol. Cell Biol.* *15*, 825–833. <https://doi.org/10.1038/nrm3903>.
- Liu, A.P. (2016). Biophysical Tools for Cellular and Subcellular Mechanical Actuation of Cell Signaling. *Biophys. J.* *111*, 1112–1118. <https://doi.org/10.1016/j.bpj.2016.02.043>.
- Norregaard, K., Metzler, R., Ritter, C.M., Berg-Sørensen, K., and Oddershede, L.B. (2017). Manipulation and Motion of Organelles and Single Molecules in Living Cells. *Chem. Rev.* *117*, 4342–4375. <https://doi.org/10.1021/acs.chemrev.6b00638>.
- Valon, L., Marín-Llauradó, A., Wyatt, T., Charras, G., and Treppe, X. (2017). Optogenetic control of cellular forces and mechanotransduction. *Nat. Commun.* *8*, 14396. <https://doi.org/10.1038/ncomms14396>.
- Rai, A.K., Rai, A., Ramaiya, A.J., Jha, R., and Mallik, R. (2013). Molecular Adaptations Allow Dynein to Generate Large Collective Forces inside Cells. *Cell* *152*, 172–182. <https://doi.org/10.1016/j.cell.2012.11.044>.
- Guet, D., Mandal, K., Pinot, M., Hoffmann, J., Abidine, Y., Sigaut, W., Bardin, S., Schauer, K., Goud, B., and Manneville, J.-B. (2014). Mechanical role of actin dynamics in the rheology of the Golgi complex and in Golgi-associated trafficking events. *Curr. Biol.* *24*, 1700–1711. <https://doi.org/10.1016/j.cub.2014.06.048>.
- van Bergeijk, P., Adrian, M., Hoogenraad, C.C., and Kapitein, L.C. (2015). Optogenetic control of organelle transport and positioning. *Nature* *518*, 111–114. <https://doi.org/10.1038/nature14128>.
- Duan, L., Che, D., Zhang, K., Ong, Q., Guo, S., and Cui, B. (2015). Optogenetic control of molecular motors and organelle distributions in cells. *Chem. Biol.* *22*, 671–682. <https://doi.org/10.1016/j.chembiol.2015.04.014>.
- Wang, Y., Barnett, S.F.H., Le, S., Guo, Z., Zhong, X., Kanchanawong, P., and Yan, J. (2019). Label-free Single-Molecule Quantification of Rapamycin-induced FKBP-FRB Dimerization for Direct Control of Cellular Mechanotransduction. *Nano Lett.* *19*, 7514–7525. <https://doi.org/10.1021/acs.nanolett.9b03364>.
- Stevens, J.M., Galyov, E.E., and Stevens, M.P. (2006). Actin-dependent movement of bacterial pathogens. *Nat. Rev. Microbiol.* *4*, 91–101. <https://doi.org/10.1038/nrmicro1320>.
- Kocks, C., Gouin, E., Tabouret, M., Berche, P., Ohayon, H., and Cossart, P. (1992). *L. monocytogenes*-induced actin assembly requires the actA gene product, a surface protein. *Cell* *68*, 521–531.
- Radoshevich, L., and Cossart, P. (2018). *Listeria monocytogenes*: towards a complete picture of its physiology and pathogenesis. *Nat. Rev. Microbiol.* *16*, 32–46. <https://doi.org/10.1038/nrmicro.2017.126>.
- Kocks, C., Hellio, R., Gounon, P., Ohayon, H., and Cossart, P. (1993). Polarized distribution of *Listeria monocytogenes* surface protein ActA at the site of directional actin assembly. *J. Cell Sci.* *105* (Pt 3), 699–710.
- Welch, M.D., Iwamatsu, A., and Mitchison, T.J. (1997). Actin polymerization is induced by Arp2/3 protein complex at the surface of *Listeria monocytogenes*. *Nature* *385*, 265–269. <https://doi.org/10.1038/385265a0>.
- Welch, M.D., Rosenblatt, J., Skoble, J., Portnoy, D.A., and Mitchison, T.J. (1998). Interaction of human Arp2/3 complex and the *Listeria monocytogenes* ActA protein in actin filament nucleation. *Science* *281*, 105–108.
- Mogilner, A., and Oster, G. (2003). Force generation by actin polymerization II: the elastic ratchet and tethered filaments. *Biophys. J.* *84*, 1591–1605. [https://doi.org/10.1016/S0006-3495\(03\)74969-8](https://doi.org/10.1016/S0006-3495(03)74969-8).
- Theriot, J.A., Mitchison, T.J., Tilney, L.G., and Portnoy, D.A. (1992). The rate of actin-based motility of intracellular *Listeria monocytogenes* equals the rate of actin polymerization. *Nature* *357*, 257–260. <https://doi.org/10.1038/357257a0>.
- Upadhyaya, A., and van Oudenaarden, A. (2003). Biomimetic systems for studying actin-based motility. *Curr. Biol.* *13*, R734–R744. <https://doi.org/10.1016/j.cub.2003.08.051>.
- Plastino, J., and Sykes, C. (2005). The actin slingshot. *Curr. Opin. Cell Biol.* *17*, 62–66. <https://doi.org/10.1016/j.cob.2004.12.001>.



28. Bieling, P., Li, T.-D., Weichsel, J., McGorty, R., Jreij, P., Huang, B., Fletcher, D.A., and Mullins, R.D. (2016). Force Feedback Controls Motor Activity and Mechanical Properties of Self-Assembling Branched Actin Networks. *Cell* 164, 115–127. <https://doi.org/10.1016/j.cell.2015.11.057>.
29. DeRose, R., Miyamoto, T., and Inoue, T. (2013). Manipulating signaling at will: chemically-inducible dimerization (CID) techniques resolve problems in cell biology. *Pflügers Archiv* 465, 409–417. <https://doi.org/10.1007/s00424-012-1208-6>.
30. Castellano, F., Montcourrier, P., Guillemot, J.C., Gouin, E., Machesky, L., Cossart, P., and Chavrier, P. (1999). Inducible recruitment of Cdc42 or WASP to a cell-surface receptor triggers actin polymerization and filopodium formation. *Curr. Biol.* 9, 351–360.
31. Upadhyaya, A., Chabot, J.R., Andreeva, A., Samadani, A., and van Oudenaarden, A. (2003). Probing polymerization forces by using actin-propelled lipid vesicles. *Proc. Natl. Acad. Sci. USA* 100, 4521–4526. <https://doi.org/10.1073/pnas.0837027100>.
32. Giardini, P.A., Fletcher, D.A., and Theriot, J.A. (2003). Compression forces generated by actin comet tails on lipid vesicles. *Proc. Natl. Acad. Sci. USA* 100, 6493–6498. <https://doi.org/10.1073/pnas.1031670100>.
33. Pagliuso, A., Cossart, P., and Stavru, F. (2018). The ever-growing complexity of the mitochondrial fission machinery. *Cell. Mol. Life Sci.* 75, 355–374. <https://doi.org/10.1007/s00018-017-2603-0>.
34. Rowland, A.A., and Voeltz, G.K. (2012). Endoplasmic reticulum-mitochondria contacts: function of the junction. *Nat. Rev. Mol. Cell Biol.* 13, 607–625. <https://doi.org/10.1038/nrm3440>.
35. Kornmann, B. (2013). The molecular hug between the ER and the mitochondria. *Curr. Opin. Cell Biol.* 25, 443–448. <https://doi.org/10.1016/j.ceb.2013.02.010>.
36. Lin, Y.-C., Nihongaki, Y., Liu, T.-Y., Razavi, S., Sato, M., and Inoue, T. (2013). Rapidly reversible manipulation of molecular activity with dual chemical dimerizers. *Angew. Chem., Int. Ed. Engl.* 52, 6450–6454. <https://doi.org/10.1002/anie.201301219>.
37. Niu, J., Ben Johny, M., Dick, I.E., and Inoue, T. (2016). Following Optogenetic Dimerizers and Quantitative Prospects. *Biophys. J.* 111, 1132–1140. <https://doi.org/10.1016/j.bpj.2016.07.040>.
38. Guntas, G., Hallett, R.A., Zimmerman, S.P., Williams, T., Yumerefendi, H., Bear, J.E., and Kuhlman, B. (2015). Engineering an improved light-induced dimer (iLID) for controlling the localization and activity of signaling proteins. *Proc. Natl. Acad. Sci. USA* 112, 112–117. <https://doi.org/10.1073/pnas.1417910112>.
39. Simon, C., Kusters, R., Caorsi, V., Allard, A., Abou-Ghali, M., Manzi, J., Di Cicco, A., Lévy, D., Lenz, M., Joanny, J.-F., et al. (2019). Actin dynamics drive cell-like membrane deformation. *Nat. Phys.* 15, 602–609. <https://doi.org/10.1038/s41567-019-0464-1>.
40. Zhu, C., Lee, C.T., and Rangamani, P. (2022). Mem3DG: Modeling membrane mechanochemical dynamics in 3D using discrete differential geometry. *Biophys. Rep.* 2, 100062. <https://doi.org/10.1016/j.bpr.2022.100062>.
41. Canham, P.B. (1970). The minimum energy of bending as a possible explanation of the biconcave shape of the human red blood cell. *J. Theor. Biol.* 26, 61–81. [https://doi.org/10.1016/S0022-5193\(70\)80032-7](https://doi.org/10.1016/S0022-5193(70)80032-7).
42. Helfrich, W. (1973). Elastic Properties of Lipid Bilayers: Theory and Possible Experiments. *Z. Naturforsch. C Biosci.* 28, 693–703. <https://doi.org/10.1515/znc-1973-11-1209>.
43. Kuo, S.C., and McGrath, J.L. (2000). Steps and fluctuations of *Listeria monocytogenes* during actin-based motility. *Nature* 407, 1026–1029. <https://doi.org/10.1038/35039544>.
44. Marcy, Y., Prost, J., Carlier, M.-F., and Sykes, C. (2004). Forces generated during actin-based propulsion: a direct measurement by micromanipulation. *Proc. Natl. Acad. Sci. USA* 101, 5992–5997. <https://doi.org/10.1073/pnas.0307704101>.
45. Youle, R.J., and van der Bliek, A.M. (2012). Mitochondrial Fission, Fusion, and Stress. *Science* 337, 1062–1065. <https://doi.org/10.1126/science.1219855>.
46. Friedman, J.R., and Nunnari, J. (2014). Mitochondrial form and function. *Nature* 505, 335–343. <https://doi.org/10.1038/nature12985>.
47. Picard, M., Shirihai, O.S., Gentil, B.J., and Burelle, Y. (2013). Mitochondrial morphology transitions and functions: implications for retrograde signaling? *Am. J. Physiol. Regul. Integr. Comp. Physiol.* 304, R393–R406. <https://doi.org/10.1152/ajpregu.00584.2012>.
48. Pernas, L., and Scorrano, L. (2016). Mito-Morphosis: Mitochondrial Fusion, Fission, and Cristae Remodeling as Key Mediators of Cellular Function. In *Annual Review of Physiology*, D. Julius, ed., p. 505.
49. Imamura, H., Nhat, K.P.H., Togawa, H., Saito, K., Iino, R., Kato-Yamada, Y., Nagai, T., and Noji, H. (2009). Visualization of ATP levels inside single living cells with fluorescence resonance energy transfer-based genetically encoded indicators. *Proc. Natl. Acad. Sci. USA* 106, 15651–15656. <https://doi.org/10.1073/pnas.0904764106>.
50. Ward, M.W. (2010). Quantitative analysis of membrane potentials. *Methods Mol. Biol.* 591, 335–351. [https://doi.org/10.1007/978-1-60716-404-3\\_20](https://doi.org/10.1007/978-1-60716-404-3_20).
51. Ermakova, Y.G., Bilan, D.S., Matlashov, M.E., Mishina, N.M., Markvicheva, K.N., Subach, O.M., Subach, F.V., Bogeski, I., Hoth, M., Enikolopov, G., and Belousov, V.V. (2014). Red fluorescent genetically encoded indicator for intracellular hydrogen peroxide. *Nat. Commun.* 5, 5222. <https://doi.org/10.1038/ncomms6222>.
52. Reitzer, L.J., Wice, B.M., and Kennell, D. (1979). Evidence that glutamine, not sugar, is the major energy source for cultured HeLa cells. *J. Biol. Chem.* 254, 2669–2676.
53. Rossignol, R., Gilkerson, R., Aggeler, R., Yamagata, K., Remington, S.J., and Capaldi, R.A. (2004). Energy substrate modulates mitochondrial structure and oxidative capacity in cancer cells. *Cancer Res.* 64, 985–993. <https://doi.org/10.1158/0008-5472.can-03-1101>.
54. Pickles, S., Vigié, P., and Youle, R.J. (2018). Mitophagy and Quality Control Mechanisms in Mitochondrial Maintenance. *Curr. Biol.* 28, R170–R185. <https://doi.org/10.1016/j.cub.2018.01.004>.
55. Yamada, T., Murata, D., Adachi, Y., Itoh, K., Kameoka, S., Igarashi, A., Kato, T., Araki, Y., Haganir, R.L., Dawson, T.M., et al. (2018). Mitochondrial Stasis Reveals p62-Mediated Ubiquitination in Parkin-Independent Mitophagy and Mitigates Nonalcoholic Fatty Liver Disease. *Cell Metab.* 28, 588–604.e5. <https://doi.org/10.1016/j.cmet.2018.06.014>.
56. Banani, S.F., Lee, H.O., Hyman, A.A., and Rosen, M.K. (2017). Biomolecular condensates: organizers of cellular biochemistry. *Nat. Rev. Mol. Cell Biol.* 18, 285–298. <https://doi.org/10.1038/nrm.2017.7>.
57. Wheeler, R.J., and Hyman, A.A. (2018). Controlling compartmentalization by non-membrane-bound organelles. *Philos. Trans. R. Soc. Lond. B Biol. Sci.* 373, 20170193. <https://doi.org/10.1098/rstb.2017.0193>.
58. Nakamura, H., Lee, A.A., Afshar, A.S., Watanabe, S., Rho, E., Razavi, S., Suarez, A., Lin, Y.-C., Tanigawa, M., Huang, B., et al. (2018). Intracellular production of hydrogels and synthetic RNA granules by multivalent molecular interactions. *Nat. Mater.* 17, 79–89. <https://doi.org/10.1038/nmat5006>.
59. Ivanov, P., Kedersha, N., and Anderson, P. (2019). Stress Granules and Processing Bodies in Translational Control. *Cold Spring Harbor Perspect. Biol.* 11, a032813. <https://doi.org/10.1101/cshperspect.a032813>.
60. Zhang, K., Daigle, J.G., Cunningham, K.M., Coyne, A.N., Ruan, K., Grima, J.C., Bowen, K.E., Wadhwa, H., Yang, P., Rigo, F., et al. (2018). Stress Granule Assembly Disrupts Nucleocytoplasmic Transport. *Cell* 173, 958–971.e17. <https://doi.org/10.1016/j.cell.2018.03.025>.
61. Schindelin, J., Arganda-Carreras, I., Frise, E., Kaynig, V., Longair, M., Pietzsch, T., Preibisch, S., Rueden, C., Saalfeld, S., Schmid, B., et al. (2012). Fiji: an open-source platform for biological-image analysis. *Nat. Methods* 9, 676–682. <https://doi.org/10.1038/nmeth.2019>.
62. Sallee, N.A., Rivera, G.M., Dueber, J.E., Vasilescu, D., Mullins, R.D., Mayer, B.J., and Lim, W.A. (2008). The pathogen protein EspF(U) hijacks actin polymerization using mimicry and multivalency. *Nature* 454, 1005–1008. <https://doi.org/10.1038/nature07170>.

63. Taslimi, A., Vrana, J.D., Chen, D., Borinskaya, S., Mayer, B.J., Kennedy, M.J., and Tucker, C.L. (2014). An optimized optogenetic clustering tool for probing protein interaction and function. *Nat. Commun.* *5*, 4925. <https://doi.org/10.1038/ncomms5925>.
64. Miyamoto, T., Rho, E., Sample, V., Akano, H., Magari, M., Ueno, T., Gorshkov, K., Chen, M., Tokumitsu, H., Zhang, J., and Inoue, T. (2015). Compartmentalized AMPK signaling illuminated by genetically encoded molecular sensors and actuators. *Cell Rep.* *11*, 657–670. <https://doi.org/10.1016/j.celrep.2015.03.057>.
65. Miyamoto, T., Rho, E., Kim, A., and Inoue, T. (2018). Cellular Application of Genetically Encoded Sensors and Impeders of AMPK. *Methods Mol. Biol.* *1732*, 255–272. [https://doi.org/10.1007/978-1-4939-7598-3\\_17](https://doi.org/10.1007/978-1-4939-7598-3_17).

## STAR★METHODS

### KEY RESOURCES TABLE

REAGENT or RESOURCE	SOURCE	IDENTIFIER
<b>Chemicals, peptides, and recombinant proteins</b>		
Rapamycin	LC Laboratories	R-5000
Latrunculin A	Sigma Aldrich	L5163
CK-666	Sigma Aldrich	SML0006
<i>Para</i> -aminoblebbistatin	AXOL	ax494682
2-deoxy-D-glucose	Sigma Aldrich	D8375
Rotenone	Sigma Aldrich	R8875
CCCP	Sigma Aldrich	C2759
Tetramethylrhodamine ethyl ester	Sigma Aldrich	87917
eBioscience Fixable Viability Dye eFluor780	Invitrogen	65-0865-14
Paraformaldehyde	EMS	15714
Glutaraldehyde	EMS	16120
Osmium tetroxide	EMS	RT19132
Potassium ferrocyanide	EMS	26604–01
Uranyl acetate	EMS	22400
<b>Experimental models: Cell lines</b>		
HeLa	ATCC	CCL-2; RRID: CVCL_0030
COS-7	ATCC	CRL-1651; RRID: CVCL_0224
U2OS	ATCC	HTB-96; RRID: CVCL_0042
NIH3T3	ATCC	CRL-1658; RRID: CVCL_0594
50B11	Charlotte Sumner	RRID:CVCL_M745
Drp1 KO mouse embryonic fibroblast	Hiroimi Sesaki	N/A
<b>Recombinant DNA</b>		
ActA(1–584)-FKBP-mCherry	This work	N/A
ActA(1–584)-SspB-mCherry	This work	N/A
6xHis-ActA(1–584)-FRB-ECFP	This work	N/A
Tom20-ECFP-FRB	This work	N/A
Tom20-EYFP-iLID	This work	N/A
Tom20-FRB	This work	N/A
Su9-EYFP	This work	N/A
EYFP-Parkin	This work	N/A
ECFP-FRB-MoA	This work	N/A
ECFP-FRB-giantinS	This work	N/A
ECFP-FRB-Sec61B	This work	N/A
EYFP-FKBP-N-WASP	This work	N/A
EYFP-FKBP-DN N-WASP	This work	N/A
EYFP-FKBP-EspFu5R	This work	N/A
EYFP-FKBP-Nck SH3	This work	N/A
ECFP-FRB-TIA1	This work	N/A
ECFP-FRB-G3BP1	This work	N/A
ECFP-FRB-FXR1b	This work	N/A

(Continued on next page)

**Continued**

REAGENT or RESOURCE	SOURCE	IDENTIFIER
EYFP-PABP1	This work	N/A
Lifeact-EYFP	This work	N/A
Lifeact-iRFP713	This work	N/A
<b>Software and algorithms</b>		
MetaMorph	Molecular Devices	N/A
Fiji	Schindelin et al. <sup>61</sup>	<a href="https://fiji.sc/">https://fiji.sc/</a>
R	The R Foundation	N/A
Python	Python Software Foundation	N/A
Custom scripts	This paper	<a href="https://github.com/RangamaniLabUCSD/ActuAtoForceEstimation">https://github.com/RangamaniLabUCSD/ActuAtoForceEstimation</a>

**RESOURCE AVAILABILITY**

**Lead contact**

Further information and requests for resources and reagents should be directed to and will be fulfilled by the lead contact, Takanari Inoue ([jctinoue@jhmi.edu](mailto:jctinoue@jhmi.edu)).

**Materials availability**

Most of the plasmids used in the manuscript will be deposited and available from Addgene, or from the corresponding authors upon reasonable request.

**Data and code availability**

- The actual data of this study are available from the corresponding authors upon reasonable request.
- The original codes used in this study are available from a private repository of the Rangamani Lab: <https://github.com/RangamaniLabUCSD/ActuAtoForceEstimation>.
- Any additional information that supports the findings of this study is available from the corresponding authors upon reasonable request.

**EXPERIMENTAL MODEL AND STUDY PARTICIPANT DETAILS**

**Cell lines used in the study**

HeLa cells, COS-7 cells, NIH3T3 cells, and U2OS cells were obtained from ATCC, and cultured in Dulbecco's modified Eagle's Medium (Corning, 10013CV) supplemented with 10% fetal bovine serum (FBS) (Sigma Aldrich, F6178) at 37°C, 5% CO<sub>2</sub>. 50B11 cells were kindly provided by Charlotte Sumner, and cultured in Neurobasal medium (Thermo Fisher, 21103049) supplemented with 5% fetal bovine serum, 0.2% v/v B27 (Thermo Fisher, 17504044), 0.1% v/v Glutamax (Thermo Fisher, 35050061), penicillin-streptomycin (Thermo Fisher, 15140163), and 0.2% w/v glucose. 50B11 cells were treated with 50 μM forskolin (Millipore Sigma, F6886) in 0.2% fetal bovine serum-containing Neurobasal medium 24 h prior to imaging, allowing the cells to change morphology into elongated, neuron-like shape with long processes. Drp1 knockout mouse embryonic fibroblasts (MEFs) were a kind gift from Hiromi Sesaki. Drp1 MEFs were cultured in 10% FBS-containing Iscove's modified Dulbecco's medium (Gibco, 12440053).

**METHOD DETAILS**

**DNA plasmids**

All the plasmids were constructed by standard subcloning techniques based either on pECFP, pEYFP, and pmCherry plasmids. ActA sequences were synthesized with codon usage optimized for mammals (Genscript). Signal sequences for specific targeting to organelles were synthesized as oligo DNAs and subcloned. TIA-1, PABP-1, G3BP1, and FXR1b sequences are PCR-amplified from constructs kindly provided by Nancy Kedersha. EspFu5R sequence<sup>62</sup> and Nck SH3 sequence<sup>63</sup> are provided by Wendell Lim and Matthew Kennedy, respectively, and PCR amplified for subcloning. N-terminal deletion of N-WASP was carried out according to a previous report,<sup>30</sup> and the resultant deletion mutant was subcloned. ATeam1.03 plasmids<sup>49</sup> and HyperRed constructs<sup>51</sup> are kindly provided by Hiroomi Imamura and Vsevolod Belousov, respectively. Major plasmids used in the manuscript will be deposited and available from Addgene.



### 6xHis-ActA (1–584)-FRB-CFP purification

ActA(1–584)-FRB-ECFP was subcloned in pET28a plasmid to have N-terminal 6x His tag for purification. We inoculated a colony of BL21-CodonPlus(DE3)-RIL competent cells (Agilent Technologies 230245) transformed with the plasmid DNA in 10 mL of LB media supplemented with kanamycin and grew overnight at 37°C, 220 rpm. The culture was transferred to 1L of LB/kanamycin and expanded at 37°C, 220 rpm until OD<sub>600</sub> reached ~0.5. The cells were induced with IPTG at a final concentration of 0.4 mM and continued culture at 19°C, 220 rpm, overnight. Cells were pelleted at 4500 x g, 4°C for 15 min and the pellet resolubilized in the lysis buffer (10 mM Tris pH 7.6, 100 mM NaCl, 10 mM imidazole, 10% glycerol, 1 mM β-mercaptoethanol and cComplete EDTA-free protease inhibitor tablet (Sigma Aldrich 11836170001)). The cells were lysed with a microfluidizer and the soluble fraction harvested by centrifugation at 16,000 x g, 4°C for 40 min. Supernatant was filtered with 0.2 μm syringe filters (Thermo Fisher F25006). A 5 mL His-Trap HP column (GE Life Sciences) was equilibrated with the lysis buffer lacking protease inhibitors and the protein eluted using a linear imidazole gradient from 50 to 500 mM over 20 column volumes. The eluted fractions were analyzed on an SDS-PAGE gel and subsequently the peak fractions detected on the Coomassie blue (BioRad 1610400) stained gel were pooled and dialyzed in a 10 kDa SnakeSkin dialysis tubing (Thermo Fisher 68100) in 2L of storage buffer (10 mM Tris-HCl pH 7.6, and 50 mM NaCl, 10% glycerol, and 1 mM β-mercaptoethanol) at 4°C, overnight. The next day the protein was dialyzed for an additional 3 h in fresh storage buffer and subsequently applied to a Superdex 200 10/300 GL (GE Life Sciences) equilibrated in the same buffer. The peak fractions were combined, and concentrated with an Amicon Ultra 10 kDa centrifugal filter unit (Millipore UFC801024). Aliquoted protein vials were flash-frozen and stored at –80°C.

### In vitro pyrene assay of actin nucleation efficiency

Rabbit skeletal muscle actin (Cytoskeleton, Inc. AKL99), pyrene-labeled actin (Cytoskeleton, Inc. AP05), Arp2/3 complex (Cytoskeleton, Inc. RP01P), and GST-WASP-VCA (Cytoskeleton, Inc. VCG03-A) were reconstituted and used as described in manufacturer's protocols except for size exclusion chromatography (GE Superdex 200 increase 10/300) purification of actin. Purified actin was stored at 4°C with dialysis against G-buffer 1 (2 mM Tris-HCl (pH 7.5 at RT), 0.1 mM CaCl<sub>2</sub>, 0.2 mM ATP, 0.5 mM DTT, 1 mM NaN<sub>3</sub>).

Pyrene-actin assay was performed by using FluoroMax 3 and polymerization kinetics were measured by using FluoroMax 3 operated by Datamax software (HORIBA, 365 nm emission 1 nm bandwidth and 497 nm excitation 5 nm bandwidth). Proteins for pyrene assay were prepared as follows. Actin and pyrene-labeled actin were diluted with G-buffer 2 (5 mM Tris-HCl (pH 7.5), 0.2 mM CaCl<sub>2</sub>) and mixed to make 5% pyrene labeled 4 μM actin solution. Arp2/3, Actuator-FRB-ECFP, and GST-WASP-VCA were diluted in F-buffer (10 mM Tris-HCl (pH 7.5 RT), 50 mM KCl, 2 mM MgCl<sub>2</sub>, 1 mM ATP). Reaction was started by mixing 28 μL of G-buffer 2, 12.5 μL of 4 μM actin (5% pyrene-labeled), 4.5 μL 10x F buffer, and 5 μL of 100 nM Arp2/3. Actuator, GST-WASP-VCA, or F-buffer (negative control) was added 5–10 min after measuring baseline.

### Cell viability assay using FACS and cell viability dye

HeLa cells were cultured and transfected with plasmids (ActA-FKBP-EGFP or FKBP-EGFP) in 6-well culture plate. After 24 h, cells were trypsinized and collected by centrifugation. Cells were then re-suspended in culture medium supplemented with eBioscience Fixable Viability Dye eFluor780 (Invitrogen) according to the manufacturer's instruction for 30 min. After staining, cells were collected and resuspended in fresh culture medium for cell sorting. In a positive control condition, cells were re-suspended in culture medium without dye and heated at 95°C for 5 min, followed by the staining. Analysis of the fluorescence was performed with a Cell Sorter MA900 (SONY). Fluorescence signals of the viability dye and EGFP were monitored through 785/60 nm and 525/50 nm band-pass filters, respectively, using 638 and 488 nm laser for excitation. Background fluorescence was monitored using HeLa cells without any staining to define the gate for fluorescence-positive fraction. Percentage of infrared fluorescence-positive events was used to evaluate the viability of cells under each condition.

### Transfection and live-cell imaging

Cells were seeded on a LabTek 8-well chamber (Thermo Scientific) coated with poly-D-lysine hydrobromide (Sigma Aldrich, P6407) solubilized in sterile water at 0.1 mg/mL. Transfection was done using X-tremegene9 transfection reagent (Roche, 6365779001) following the manufacturer's instruction, unless specified. Ratio amount between plasmids used for transfection was adjusted so that plasmids coding Actuator were relatively less (10–50% of organelle or stress granule markers), which resulted in efficient translocation of the Actuator peptides. Organelle markers or signal sequences used for translocation to mitochondria, Golgi apparatus, and outer nuclear envelope/endoplasmic reticulum were derived from Tom20, Giantin, and Sec61B proteins, respectively. As an exception, mitochondria translocation in 50B11 cells was carried out with signal sequences of MoA protein, as Tom20 signal sequence functioned poorly in this cell type.

Cells were imaged 24 h after transfection. For live-cell imaging of organelle deformation, Eclipse Ti inverted fluorescence microscope (Nikon) equipped with ×60 oil-immersion objective lens (Nikon) and Zyla 4.2 plus CMOS camera (Andor) was used, unless specified. The system was controlled by NIS element software (Nikon). Stage-top incubator (Tokai Hit) was used to incubate samples at 37°C, 5% CO<sub>2</sub> during imaging. For chemical stimulation, 100 μM rapamycin (LC Laboratories, R-5000) stock in DMSO was diluted in extracellular medium and used at final concentration of 100 nM. Interval between consecutive frames was either five or 10 s.

### Quantification of mitochondria deformation

A region with readily observable mitochondria morphology was chosen as a region of interest (ROI) in each cell analyzed. Fluorescence images of mitochondria marker within ROIs were then processed by “top-hat morphology filter” in MetaMorph software (Molecular Devices). Morphology filtered images were binarized, and skeletonized using Fiji software (ImageJ). The skeletonized mitochondria morphology was analyzed by “analyze skeleton” menu of the software, and “the length of the longest shortest path” was extracted for each mitochondrion. The resultant lengths were averaged over each ROI to obtain mean mitochondria lengths in the formula shown in [Figure 1C](#), using mitochondria images within the same region before and after stimuli.

### Confocal imaging and optogenetic stimulation

Light-inducible version of Actuator was imaged with LSM800 confocal microscope (Zeiss) using 514 nm and 561 nm lasers to excite EYFP and mCherry, respectively. To induce dimerization between iLID and SspB, 488 nm laser was used, taking advantage of the bleaching function in Zen Black software (Zeiss). In order to avoid background dimerization, 514 nm laser intensity was kept as low as possible during EYFP imaging. Samples were incubated at 37°C, 5% CO<sub>2</sub> using a built-in stage-top incubator during imaging.

### Three-dimensional confocal imaging

HeLa cells were grown in glass-bottom chamber and transfected with plasmids the day before fixation. Cells were stimulated with rapamycin for 30 min and fixed by 4% PFA before imaging. Three-dimensional imaging was performed with a laser-scanning confocal microscope sp8 (Leica) equipped with white laser and HyD detector array, using ×63 oil-immersion objective lens (Leica). The three-dimensional image stack was deconvoluted using the Lightning mode of LAS-X software (Leica).

### Correlative electron microscopy

Correlative light and TEM images were obtained according to the protocol described in a previous study.<sup>52</sup> Briefly, cells were cultured on sapphire disks that are carbon-coated with a grid pattern. This pattern was used to locate the region of interest in an electron microscope. Cells were fixed with 4% paraformaldehyde prior to fluorescence imaging. Following fluorescence imaging, cells were further fixed with 2% glutaraldehyde, 1 mM CaCl<sub>2</sub>, and 0.1 M cacodylate buffer, pH 7.4, for 1 h on ice. Samples were then post-fixed in 1% OsO<sub>4</sub>, 1% potassium ferrocyanide and 0.1 M cacodylate buffer, for 1 h on ice. After dehydration with 50, 70, 90, and 100% ethanol, samples were embedded into epon-araldite resin and cured for 72 h at 60°C. The regions-of-interest were located based on the grid pattern. The plastic block was trimmed to the regions-of-interest and sectioned on a diamond knife using an ultramicrotome (Leica UC7). Approximately 40 consecutive sections (40 nm each) were collected onto the pioloform-coated grids and post-stained with 2.5% uranyl acetate in 50% methanol. Samples were observed using an H-7600 transmission electron microscope (Hitachi) equipped with a dual CCD camera (Advanced Microscopy Techniques). Images were processed with FIJI software and Photoshop 2022 (Adobe). The raw images are available upon request.

### Estimation of force generated by Actuator

TEM images of deformed nuclei were used to theoretically estimate the force density distribution underlying the deformation. Details of the force estimation are described in the [Supplementary Information](#).

### FRAP measurement and analysis

FRAP measurement of Su9-EYFP was done by line-scan mode of LSM800 confocal microscope and Zen Black software (Zeiss) to observe the fast recovery kinetics after photobleaching. The bleaching function of the same software was used for photobleaching with 514 nm laser, which was also used for EYFP imaging at lower intensity. Photobleaching aimed at a single spot located in the middle of the line across which the laser scanned for imaging. To analyze the data, a Region of three pixels in width, which contained the photobleached spot in the middle, was used as a ROI. Each transient of integrated intensity over the ROI was fitted to the exponential function shown in [Figure 5C](#), using R software (the R Foundation), to obtain three fitting parameter values, *a*, *b*, and *c*.

### Fluorescence imaging of mitochondria functions

Cells were seeded on a coverslip coated by poly-D-lysine hydrobromide and cultured in 6-well culture plates. All experiments were performed with two groups of cells cultured in distinct media for 48–72 h prior to the imaging; glucose medium and galactose medium. We here refer to the conventional DMEM containing 25 mM glucose as glucose medium, while galactose medium contained 10 mM galactose in place of glucose. It has been reported that cells cultured in glucose medium metabolize the majority of glucose via glycolysis, while in galactose medium, ATP synthesis through the citrate cycle and mitochondrial respiration rate are increased.<sup>52,53</sup> Imaging was performed with an inverted fluorescence microscope, Axiovert 135 TV (Zeiss) equipped with a QIClick charge-coupled device camera (Qimaging).

For ATP measurement in mitochondria matrix, a mitochondria-targeted FRET-based ATP biosensor, mitAT1.03 was used.<sup>49</sup> Transfection was performed in the 6-well culture plate using FuGene-HD (Promega, E2311) following the manufacturer’s instructions. Fluorescence was measured by drawing three circular ROIs at mitochondria and 3 ROIs for background fluorescence. The net

fluorescence was calculated by taking the difference of the averages. Methods for Analyses of FRET ratio change are described in previous reports.<sup>64,65</sup> In glucose medium condition, 25 mM of 2-deoxy-D-glucose was used to lower ATP level as a control. In galactose medium condition, 500 nM rotenone was used instead.

To measure membrane potential across mitochondria inner membrane, tetramethylrhodamine ethyl ester (TMRE) staining dependent on the membrane potential across the membrane was used. Staining was performed at 7 nM final concentration of TMRE for HeLa cells, while 35 nM TMRE was used for COS-7 cells. As a control, a proton ionophore, carbonyl cyanid *m*-chlorophenyl hydrazone (CCCP) was used to abolish the membrane potential at a final concentration of 10  $\mu$ M. Instead of Actuator containing mCherry used in the majority of experiments described in the current report, we used EYFP-labeled Actuator in the TMRE and HyperRed experiments described below.

In ROS concentration measurement experiments, we used a mitochondria matrix-targeted ROS biosensor, HyperRed-mito.<sup>51</sup> As a control, 10 mM H<sub>2</sub>O<sub>2</sub> was used for glucose medium experiments, while 500 nM rotenone was used for galactose experiments. As a negative control peptide, C199S mutant of HyperRed-mito,<sup>51</sup> which we denoted as NC indicator, was used.

### Stress granule dispersion

Live-cell imaging of stress granule dispersion was performed in COS-7 cells, with the same experimental setups for organelle deformation experiments described above, while longer interval between frames of 1 min was adopted according to the slower kinetics observed. To form stress granules, cells were treated with 0.5 mM sodium arsenite contained in culture medium for 30 min prior to the imaging. During imaging, cells were incubated in the stage-top incubator in the sodium arsenite-containing culture medium. As a stimulus, rapamycin was manually added at the final concentration of 100 nM.

To quantify the dispersion induced by Actuator, fluorescence intensity of an independently co-expressed stress granule marker, EYFP-PABP1 was used. Regions with typical stress granules were selected as ROIs in the first frame for the analysis on MetaMorph software. The threshold was then manually adjusted to define the area of granules in the same frame. EYFP-PABP1 fluorescence images in all frames were binarized based on the threshold to create binarized masks. Cytosolic EYFP-PABP1 fluorescence intensity outside granules was also defined as a background level for subtraction. Background-subtracted fluorescence intensity was then integrated over stress granule area based on the mask images, resulting in an integrated signal within granules. The integrated signal was normalized to the values before rapamycin administration for quantification.

### Quantification and statistical analysis

Statistical parameters including the definition and exact values of N (number of cells and experiments) and deviation are reported in figures and corresponding legends. Data are represented as mean  $\pm$  SD. Welch's *t*-tests were performed in Microsoft Excel. Other statistical tests, Mann-Whitney U tests, Tukey HSD tests, and Steel-Dwass tests were performed in R software.